

A nonlocal optimization method for computational inverse design in nanophotonics

Jiaxin Zhang

Computer Science and Mathematics Division, Oak Ridge National Laboratory

Sirui Bi

Department of Civil and Systems Engineering, Johns Hopkins University

Guannan Zhang

Computer Science and Mathematics Division, Oak Ridge National Laboratory

Abstract

We propose a nonlocal optimization method for inverse design in nanophotonics. Existing local-gradient-based optimization approaches lack nonlocal exploration ability required for escaping from local minima in non-convex landscapes. A nonlocal gradient operator using directional Gaussian smoothing (DGS) is proposed to address this challenge in photonics device design. Compared with the local gradient, the DGS gradient allows for a large smoothing radius to capture the global structure of loss landscapes. A deterministic Gauss-Hermite quadrature is used to develop a DGS gradient estimator with higher accuracy than Monte Carlo estimators. The nonlocal optimization method using DGS gradient has its advantages on portability and flexibility to naturally incorporate the parameterization, physics simulation, and objective formulation together to build up an effective inverse design workflow. An adaptive smoothing radius and learning rate with quadratic decay are proposed to improve robustness and convergence within the DGS gradient optimization. To enable a clear binarized design, a dynamic growth mechanism is imposed on the projection strength in parameterization. The proposed methodology is demonstrated by an example of wavelength demultiplexer. Our method shows superior performance with faster convergence compared

Email addresses: zhangj@ornl.gov (Jiaxin Zhang), sbi2@jhu.edu (Sirui Bi), zhangg@ornl.gov (Guannan Zhang)

This manuscript has been co-authored by UT-Battelle, LLC, under contract DE-AC05-00OR22725 with the US Department of Energy (DOE). The US government retains and the publisher, by accepting the article for publication, acknowledges that the US government retains a nonexclusive, paid-up, irrevocable, worldwide license to publish or reproduce the published form of this manuscript, or allow others to do so, for US government purposes. DOE will provide public access to these results of federally sponsored research in accordance with the DOE Public Access Plan (<http://energy.gov/downloads/doe-public-access-plan>).

with classical approaches. Given varying initialization with Gaussian random noise, the optimized design using the nonlocal DGS gradient demonstrates high robustness and low uncertainty. By incorporating volume constraints into optimization, the optimized design using nonlocal method achieves an equivalently high performance but significantly reduces the amount of material usage in wavelength demultiplexer design.

Keywords: Inverse design, nanophotonics, nonlocal optimization, directional Gaussian smoothing, robustness, constrained optimization

1. Introduction

Photonic devices have been applied in a wide range of applications, including photonic integrated circuits [1], optical interconnects and sensors [2, 3], augmented reality (AR) [4] and quantum computing [5]. As a growing number of applications in nanophotonic devices, photonic design is becoming increasingly demanding and challenging to optimize the device performance [6, 7, 8, 9]. Classical design approaches based on analytical theory and intuition, however, are limited in small design space and relatively simple parameter tuning by hand. Capitalizing on the increased degrees of freedom in design space, nanophotonic devices have been designed with novel functionalities, high performance, efficiencies, and robustness that have been proven difficult to implement in traditional intuition-based methods [10].

There recently have been significant interests in using *computational inverse design* approaches to explore the full design space of novel photonic devices with a broad variety of applications [11, 12, 13, 14, 15, 16, 17, 18, 19, 20, 21]. Much of this progress is made by the gradient-based algorithm, which is a promising method to efficiently search the enormous degrees of freedom in high-dimensional design space. The gradient-based optimization typically relies on adjoint method [22, 23], which is a technique that enables the local gradient of an objective function and constraints to be calculated with respect to arbitrarily large design variables using forward physical simulation such as electromagnetic simulations. To this end, several recent studies further use automatic differentiation and backpropagation tools that are beneficial from machine learning research, to efficiently evaluate the local gradient by reducing the number of simulations [17, 24, 11, 25]. These approaches make a feasible gradient-based design of photonic structures, particularly nanophotonic devices, with better efficiency and smaller footprints than traditional devices.

Up to now, most of the studies use local gradient-based approaches for inverse design, so the optimized devices converge to a local minimum with respect to the design parameters. In many electromagnetic design problems, their landscapes have been proven to be highly nonlinear and non-convex such that many possible local minima exist [7, 11]. These local minima

depend on the initialization and vary largely as the initial conditions change. These challenges in gradient-based approaches have attracted much attention [26, 27, 28, 11]. In practice, one common way is to run an optimization several times with different initial conditions that provide a rough estimate of the device performance. However, this approach has limitations in maximizing device performance and computational efficiency, and meanwhile, it possibly gives rise to a large variety of design performance. In addition, for complicated non-convex objective functions and constraints, gradient estimation relies on the adjoint method may be either not easily accessible or unreliable. Sometimes, additional efforts are required to derive the sensitivity analysis if unusual objectives or constraints are incorporated into the optimization formulation even though the existing gradient-based scheme has been used in device design.

In principle, it is feasible to optimize the photonic devices directly by changing the value of permittivity distribution at every point. However, it is more critical to impose fabrication constraints into optimization workflow because a fundamental challenge in nanophotonic device design is that arbitrary permittivity distribution, such as very tiny feature and grey-scale value, can not be fabricated in practice [23, 29, 30]. The difficulty is often addressed by choosing an appropriate parameterization via a series of transformations that are simply an operation that affects the state of optimization. The use of transformation allows different parameterization and optimization stages to be easily swapped in and out for one another. This requires the optimizer has the capability of naturally integrating transformation into the design process. Another common constraint in optimizing material layout is the material usage (or volume fraction) in device design. In other words, it is desirable to use fewer materials but able to achieve performance that is as good as the target. To the author’s knowledge, relatively few studies have accounted for the problem of inverse design with volume constraint in nanophotonic design. One possible solution is to add a penalty term into objective function and thus convert the unconstrained optimization to constrained optimization through the augmented Lagrangian formalism. However, the penalty coefficient is very sensitive and typically difficult to control in practical implementation.

In this work, we use nonlocal optimization to develop a novel inverse design framework for nanophotonic devices. Existing gradient-based approaches lack nonlocal exploration ability required for escaping from local minima in non-convex landscapes. A nonlocal gradient operator with directional Gaussian smoothing (DGS) is proposed to address this challenge. The DGS gradient operator is achieved by investigating 1D nonlocal explorations along with d orthogonal directions and each of which defines a nonlocal directional derivative as a 1D integral. Compared with the local gradient method, the directional smoothing allows for a large smoothing radius to capture the global structure of loss landscapes. A deterministic

Gauss-Hermite (GH) quadrature is used to guarantee higher accuracy than random Monte Carlo sampling. Within the DGS scheme, a series of adaptive strategies for radius and learning rate are proposed to improve the computational efficiency, robustness, and performance. By taking the fabrication constraints into account, a dynamic growth mechanism is imposed on the projection strength in parameterization. The proposed novel inverse design framework is demonstrated by a design example of wavelength demultiplexers.

The paper is structured as follows. Section 2 provides a brief mathematical formulation and overview of inverse design. Section 3 presents the DGS gradient operator in principle and explain how DGS gradient optimization can overcome the challenges and difficulties in the local gradient optimization approaches. In Section 4, we show an example of designing wavelength demultiplexers, explain the implementation of nonlocal optimization method using DGS gradient in detail, and demonstrate the strength and advantages via the discussion and comparison. Finally, we provide a brief conclusion and discussion of future work.

2. Mathematical formulation of inverse design

This section provides a brief overview of the mathematical foundations behind the inverse design in photonic devices. Although the exact optimization problem may vary from case to case, the photonic design generally shares a similar set of features and steps, which include formulating an optimization problem, incorporating fabrication constraints and parameterization, and solving the inverse problem by optimization.

2.1. Optimization problem formulation

A general electromagnetic design problem can be cast into the following optimization formulation:

$$\begin{aligned} \min_{\mathbf{x}} \quad & f(\mathbf{E}_1, \dots, \mathbf{E}_n, \boldsymbol{\epsilon}_1, \dots, \boldsymbol{\epsilon}_n, \mathbf{x}) \\ \text{subject to} \quad & g_j(\mathbf{x}) = 0, \quad j = 1, \dots, m \\ & h_k(\mathbf{x}) \leq 0, \quad k = 1, \dots, l \end{aligned} \tag{1}$$

where \mathbf{E}_i is the electric field corresponding to the permittivity distribution $\boldsymbol{\epsilon}_i$, which depends on a parameterization vector $\mathbf{x} \in \mathbb{R}$, and f is the objective function that defines the target of the optimization. A typical objective is to maximize the transmission, which is equivalent to minimize the negative

$$f_{obj}(\mathbf{x}) = -|\mathbf{c}^\dagger \mathbf{E}(\boldsymbol{\epsilon}(\mathbf{x}))|^2 \tag{2}$$

where $\mathbf{c}^\dagger \mathbf{E}$ means the overlap integrals to compute the model coupling efficiency of the electric field \mathbf{E} with the target mode at the output. $h_k(\mathbf{x})$ in Eq. (1) are inequality constraints on \mathbf{x} , particularly fabrication and volume of materials constraints. The optimization problem in

Eq. (1) is also subject to equality constraints $g_j(\mathbf{x})$, which is referred to as that the electric fields \mathbf{E}_i generated by the input permittivity distribution $\epsilon(\mathbf{x})$ should satisfy the Maxwell’s equations in the frequency domain,

$$\nabla \times \frac{1}{\mu} \nabla \times \mathbf{E}_i - \omega_i^2 \epsilon(\mathbf{x}) \mathbf{E}_i = -i\omega_i \mathbf{J}_i \quad (3)$$

where $i = 1, \dots, n$ is the input modes, ω_i is the angular frequency, μ is the magnetic permeability of free space and \mathbf{J}_i is the input source which injects the current mode into the input waveguide. Eq. (3) is often solved by electromagnetic simulation using the finite-difference frequency-domain (FDFD) method [31] or finite-difference time-domain (FDTD) method [32].

2.2. Parameterization and constraints in optimization

Solving the optimization problem defined in Eq. (1) led to continuously varying features of $\epsilon(\mathbf{x})$, which is difficult for fabricating devices in practice. This is because the fabricated devices are typically composed of distinct materials so the permittivity can only take on certain discrete values and must keep the same along the vertical direction in fabrication with top-down lithography. A minimum feature size is another essential fabrication constraint. It is therefore critical to describe the permittivity distribution through a *parameterization* that addresses the fabrication challenges in device design [11].

Parameterization basically consists of two key components: *projection* operator and *filtering* operator. Projection operator aims to convert the continuous features to a binary feature that better captures a clear “0-1” design, where “0” represents a *background* material and “1” represents a *foreground* material in permittivity distribution. This can be achieved by defining an operator through the equation

$$\epsilon(\mathbf{x}) = \epsilon_b(\mathbf{x}) + \mathbb{H}(\varphi(\mathbf{x})) \quad (4)$$

where $\epsilon_b(\mathbf{x})$ is a permittivity background (constant) and $\varphi(\mathbf{x})$ is a 2D slice of the permittivity distribution and ranges from 0 to 1. A possible projection operator \mathbb{H} is using nonlinear penalty methods [22, 13]. Filtering operator is often used to eliminate very tiny features and avoid to the formation of checker-board pattern in material layout [33]. For example, level set methods [34, 35] construct a fabrication constraint penalty function for geometry representation of the devices. Using an appropriate parameterization, the fabrication constraints $h_k(\mathbf{x})$ can be imposed and naturally perform a binary device design.

Another common constraint in optimizing material layout is the volume fraction of

material usage, which is defined by

$$h_k(\mathbf{x}) = V(\mathbf{x})/V_0 - \gamma \leq 0 \quad (5)$$

where V and V_0 are the expected material volume and design domain volume respectively, and γ is the specific volume fraction. A simple solution of incorporating volume constraints into optimization is to add penalty terms into objective function and thus convert to unconstrained optimization so that a number of algorithms, for example, gradient descent, Adam, etc. can be used. However, the penalty coefficient, in fact, is very sensitive and difficult to determine in practical implementation.

2.3. Solving the inverse design problem

The inverse design problem can be defined to find the best permittivity distribution ϵ and the corresponding electric field \mathbf{E}_i to maximize the device performance described by the objective function in Eq. (1) and simultaneously satisfy the physics constraints in Eq. (3), fabrication constraints in Eq. (4) and material volume constraints in Eq. (5). It is a challenging task to solve this kind of constrained optimization problem that involves large-scale, high-dimensional design degrees of freedom and a highly non-convex and non-linear landscape [36, 11]. Many recent efforts have been made to develop gradient-based optimization techniques for addressing the challenges [37, 11].

To perform gradient-based optimization, the gradient $df_{obj}/d\mathbf{x}$ is required. Note that \mathbf{E}_i and ϵ_i can be complex-valued. Suppose the objective function f is real-valued, the gradient can be computed by

$$\frac{df_{obj}}{d\mathbf{x}} = \frac{\partial f_{obj}}{\partial \mathbf{x}} + 2\mathcal{R} \left[\sum_i \left(\frac{\partial f_{obj}}{\partial \mathbf{E}_i} \frac{d\mathbf{E}_i}{d\mathbf{x}} + \frac{\partial f_{obj}}{\partial \epsilon_i} \frac{d\epsilon_i}{d\mathbf{x}} \right) \right] \quad (6)$$

where $\mathcal{R}[\cdot]$ denotes taking the real part. The derivative terms $\partial f_{obj}/\partial \mathbf{E}_i$, $\partial f_{obj}/\partial \epsilon_i$ and $d\epsilon_i/d\mathbf{x}$ depend on the form of the objective function but $d\mathbf{E}_i/d\mathbf{x}$ is always required in electromagnetic simulation. It is therefore necessary to derive the gradient for FDFD or other simulation methods. Differentiating the FDFD shown in Eq. (3) through by ϵ_i , it gives

$$(\Omega - \omega^2 \text{diag}(\epsilon)) \frac{d\mathbf{E}}{d\epsilon} = \omega^2 \text{diag}(\mathbf{E}) \quad (7)$$

where Ω is the discretized version of the $\nabla \times \mu^{-1} \nabla \times$ operator. Thus,

$$\frac{d\mathbf{E}_i}{d\mathbf{x}} = \frac{d\mathbf{E}_i}{d\epsilon_i} \frac{d\epsilon_i}{d\mathbf{x}} = (\Omega - \omega_i^2 \text{diag}(\epsilon_i))^{-1} \omega_i^2 \text{diag}(\mathbf{E}_i) \frac{d\epsilon_i}{d\mathbf{x}}. \quad (8)$$

Note that, the computing in Eq. (8) is often computationally intensive because it requires the same number of electromagnetic simulations as the number of design degrees of freedom. Thanks to the development of automatic differentiation techniques in machine learning [38, 39], efficient implementation relies on automatic differentiation and backpropagation are introduced to reduce the computational cost [37, 24, 11].

3. The DGS gradient for nonlocal optimization

In this section, we describe the DGS gradient operator that was developed in our previous work [40]. To better explain the direction Gaussian smoothing strategy, we briefly recall the standard Gaussian smoothing [41] for estimating local gradients. Specifically, it starts by defining a smoothed loss function

$$F_\sigma(\mathbf{x}) = \mathbb{E}_{\mathbf{u} \sim \mathcal{N}(0, \mathbf{I}_d)} [F(\mathbf{x} + \sigma \mathbf{u})],$$

where $\mathcal{N}(0, \mathbf{I}_d)$ is the d -dimensional standard Gaussian distribution, and $\sigma > 0$ is the smoothing radius. $F_\sigma(\mathbf{x})$ inherits many characteristics from $F(\mathbf{x})$, e.g., convexity, the Lipschitz constant. Then, the gradient $\nabla F_\sigma(\mathbf{x})$ can be represented as an expectation and estimated by drawing M random samples $\{\mathbf{u}_m\}_{m=1}^M$ from $\mathcal{N}(0, \mathbf{I}_d)$, i.e.,

$$\nabla F_\sigma(\mathbf{x}) = \frac{1}{\sigma} \mathbb{E}_{\mathbf{u} \sim \mathcal{N}(0, \mathbf{I}_d)} [F(\mathbf{x} + \sigma \mathbf{u}) \mathbf{u}] \approx \frac{1}{M\sigma} \sum_{m=1}^M F(\mathbf{x} + \sigma \mathbf{u}_m) \mathbf{u}_m. \quad (9)$$

The Monte Carlo (MC) estimator in Eq. (9) is substituted into any gradient-based algorithm to update the state \mathbf{x} . *The major drawback is that the error of the MC estimator in Eq. (9) is on the order of $\varepsilon \sim \mathcal{O}(d\sigma/\sqrt{M})$.* When the dimension d is large (e.g., on the order of thousands) and the computing budget (the upper bound of M) is given, practitioners often have to sacrifice a nonlocal smoothing effect (with a relatively big σ) that helps skipping local minima to achieve a required accuracy. In other words, Eq. (9) is mostly used in the local regime with a small value for σ .

3.1. The nonlocal DGS gradient operator

The DGS gradient was developed to alleviate the above challenge with the standard Gaussian smoothing. The key idea behind the DGS gradient is to conduct 1D nonlocal explorations along d orthogonal directions in \mathbb{R}^d , each of which defines a nonlocal directional derivative as a 1D integral. The Gauss-Hermite quadrature, instead of MC sampling, is used to estimate the d 1D integrals to achieve high accuracy.

Specifically, we first define a 1D cross section of $F(\mathbf{x})$ as

$$G(y | \mathbf{x}, \boldsymbol{\xi}) = F(\mathbf{x} + y \boldsymbol{\xi}), \quad y \in \mathbb{R},$$

where \mathbf{x} is the current state of $F(\mathbf{x})$ and $\boldsymbol{\xi}$ is a unit vector in \mathbb{R}^d . The Gaussian smoothing of $G(y)$, denoted by $G_\sigma(y)$, is defined by

$$G_\sigma(y | \mathbf{x}, \boldsymbol{\xi}) := \frac{1}{\sqrt{2\pi}} \int_{\mathbb{R}} G(y + \sigma v | \mathbf{x}, \boldsymbol{\xi}) e^{-\frac{v^2}{2}} dv = \mathbb{E}_{v \sim \mathcal{N}(0,1)} [G(y + \sigma v | \mathbf{x}, \boldsymbol{\xi})]. \quad (10)$$

This is also the Gaussian smoothing of $F(\mathbf{x})$ along the direction $\boldsymbol{\xi}$ in the neighbourhood of \mathbf{x} . The derivative of $G_\sigma(y | \mathbf{x}, \boldsymbol{\xi})$ at $y = 0$ can be represented by a 1D integral

$$\mathcal{D}[G_\sigma(0 | \mathbf{x}, \boldsymbol{\xi})] = \frac{1}{\sigma} \mathbb{E}_{v \sim \mathcal{N}(0,1)} [G(\sigma v | \mathbf{x}, \boldsymbol{\xi}) v], \quad (11)$$

where $\mathcal{D}[\cdot]$ denotes the differential operator. We emphasize that Eq. (11) is fundamentally different from the directional derivative of $F_\sigma(\mathbf{x})$, because $G_\sigma(0 | \mathbf{x}, \boldsymbol{\xi})$ only conducts the directional smoothing along $\boldsymbol{\xi}$. For a matrix $\boldsymbol{\Xi} := (\boldsymbol{\xi}_1, \dots, \boldsymbol{\xi}_d)$ consisting of d orthonormal vectors, we can define d directional derivatives like those in Eq. (11) and assemble our DGS gradient as

$$\nabla_{\sigma, \boldsymbol{\Xi}}[F](\mathbf{x}) := \left[\mathcal{D}[G_\sigma(0 | \mathbf{x}, \boldsymbol{\xi}_1)], \dots, \mathcal{D}[G_\sigma(0 | \mathbf{x}, \boldsymbol{\xi}_d)] \right] \boldsymbol{\Xi}, \quad (12)$$

where the orthogonal system $\boldsymbol{\Xi}$ and the smoothing radius σ can be adjusted during an optimization process.

The next step is to develop an accurate DGS estimator. We exploit that each component of $\nabla_{\sigma, \boldsymbol{\Xi}}[F](\mathbf{x})$ only involves a 1D integral, such that the Gauss-Hermite quadrature rule [42, 43] can be used to approximate the integrals with high accuracy (shown in Eq. (14)). By doing a simple change of variable in Eq. (11), the GH rule can be directly used to obtain the following estimator for each directional derivative $\mathcal{D}[G_\sigma(0 | \mathbf{x}, \boldsymbol{\xi})]$ in Eq. (11)

$$\tilde{\mathcal{D}}^M[G_\sigma(0 | \mathbf{x}, \boldsymbol{\xi})] = \frac{1}{\sqrt{\pi}\sigma} \sum_{m=1}^M w_m F(\mathbf{x} + \sqrt{2}\sigma v_m \boldsymbol{\xi}) \sqrt{2}v_m, \quad (13)$$

where $\{v_m\}_{m=1}^M$ are the roots of the M -th order Hermite polynomial and $\{w_m\}_{m=1}^M$ are quadrature weights. Both v_m and w_m can be found online² or in [43]. Compared with MC

²Nodes and weights for GH quadrature: <https://keisan.casio.com/exec/system/1281195844>

sampling, the error of Eq. (13) can be bounded by

$$|(\tilde{\mathcal{D}}^M - \mathcal{D})[G_\sigma]| \leq C \frac{M! \sqrt{\pi}}{2^M (2M)!} \sigma^{2M-1}, \quad (14)$$

where $M!$ is the factorial of M and the constant $C > 0$ is independent of M and σ . Applying the GH quadrature rule $\tilde{\mathcal{D}}^M$ to each component of $\nabla_{\sigma, \Xi}[F](\mathbf{x})$ in Eq. (12), we define the following estimator:

$$\tilde{\nabla}_{\sigma, \Xi}^M[F](\mathbf{x}) = \left[\tilde{\mathcal{D}}^M[G_\sigma(0 | \mathbf{x}, \xi_1)], \dots, \tilde{\mathcal{D}}^M[G_\sigma(0 | \mathbf{x}, \xi_d)] \right] \Xi. \quad (15)$$

The DGS estimator has the following features:

- *Nonlocality*: The directional smoothing allows for a large radius σ to capture global structures of loss landscapes and help escape from local minima.
- *Accuracy*: The GH quadrature with the error bounded in Eq. (14) provides an estimator having much higher accuracy than MC, even when a large smoothing radius σ is used.
- *Portability*: The DGS gradient can be integrated into a majority of gradient-based algorithms, e.g., gradient descent, Adam, and those with constraints.
- *Scalability*: The DGS estimator in Eq. (15) requires $M \times d$ evaluations of $F(\mathbf{x})$, and these evaluations are completely parallelizable as those in random sampling.

3.2. High-dimensional function demonstration

To illustrate the performance of the DGS gradient, we combine the DGS gradient with the standard gradient descent algorithm to optimize the 1000D Ackley function, which is one of the benchmark functions used to test non-convex optimization algorithms [44, 45]. The Ackley function is defined by

$$F(\mathbf{x}) = -a \exp \left(-b \sqrt{\frac{1}{d} \sum_{i=1}^d x_i^2} \right) - \exp \left(\frac{1}{d} \sum_{i=1}^d \cos(cx_i) \right) + a + \exp(1), \quad (16)$$

where d is the dimension and $a = 20, b = 0.2, c = 2\pi$ are used in our experiments. The input domain $\mathbf{x} \in [-32.768, 32.768]$. The global minimum is $f(\mathbf{x}^*) = 0$, at $\mathbf{x}^* = (0, \dots, 0)$. The Ackley function represents non-convex landscapes with nearly flat outer region. The function poses a risk for optimization algorithms, particularly hill-climbing algorithms, to be trapped

in one of its many local minima. At each iteration, we update the state \mathbf{x}_t to \mathbf{x}_{t+1} by

$$\mathbf{x}_{t+1} = \mathbf{x}_t - \lambda_t \tilde{\nabla}_{\sigma_t, \Xi}^M [F](\mathbf{x}_t), \quad (17)$$

where $\Xi = \mathbf{I}_d$. The learning rate λ_t follows a polynomial decay schedule $\lambda_t = (\lambda_0 - \lambda_T) \left(1 - \frac{t}{T}\right)^\tau + \lambda_T$ with $\lambda_0 = 4000$, $\lambda_T = 0.001$, $\tau = 4$, $T = 60$. The smoothing radius also follows a polynomial decay schedule $\sigma_t = (\sigma_0 - \sigma_T) \left(1 - \frac{t}{T}\right)^\nu + \sigma_T$ with $\sigma_0 = 2.0$, $\sigma_T = 0.001$, $\nu = 2.0$. We compare our method with the standard Gaussian smoothing method (i.e., replacing $\tilde{\nabla}_{\sigma_t, \Xi}^M [F](\mathbf{x}_t)$ with Eq. (9)), the BFGS method, and the finite difference method for estimating local gradients. The result is shown in Figure 1. As shown in Figure 1(Left), the Ackley function has many local minima which pose significant challenges for optimization. Figure 1 (Right) shows that the DGS gradient exploited its nonlocal exploration ability to skip the local minima and converge to the global minimum. The other baseline methods do not converge because they are trapped in some local minima.

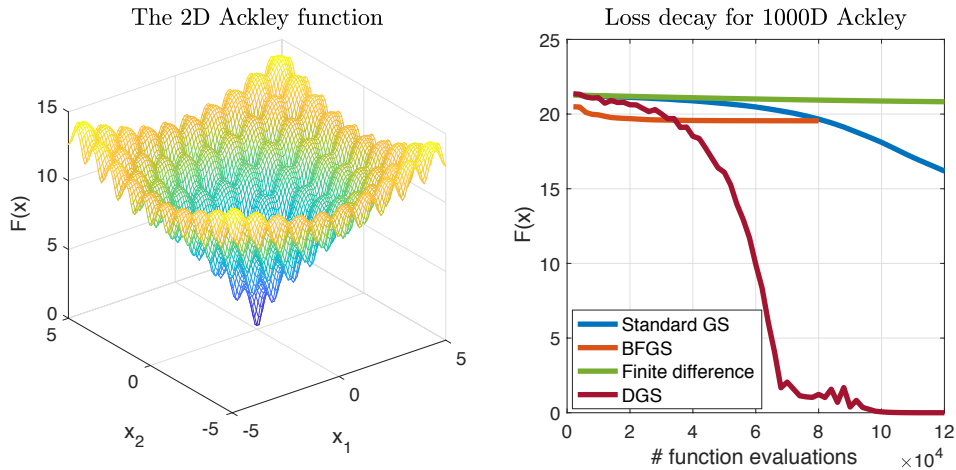


Figure 1: (Left) The landscape of the 2D Ackley function that possesses many local minima. (Right) Comparison of the loss decay w.r.t. # function evaluations for the 1000D Ackley function. Each curve was generated by averaging 20 independent trials with random initial states. The global minimum is $F(\mathbf{x}) = 0$. DGS gradient successfully found the global minimum while the other baselines are trapped in local minima.

4. Inverse design of wavelength demultiplexer

In this section, we use DGS-based nonlocal optimization method to design wavelength demultiplexer in 3D. This example is a canonical benchmarking demonstration for inverse design in nanophotonic devices. We first provide a problem description with an objective function definition and parameterization scheme. Then a methodology workflow illustrates how to incorporate DGS gradient optimization for inverse design. Finally, we demonstrate the superior performance of the optimized device using nonlocal optimization method, investigate

the effect of random initialization on robustness, and conduct constrained optimization with a limited amount of materials.

4.1. Problem description

As shown in Figure 2, we choose a three-port structure with 500 nm input waveguide and output waveguides and a square $2.5 \mu\text{m} \times 2.5 \mu\text{m}$ design region. We design a device for the 220 nm silicon-on-insulator (SOI) platform where the structure is constrained to a single fully etched Si layer on a SiO_2 substrate with air cladding. For illustration, the refractive indices of $n_{\text{air}} = 1$, $n_{\text{SiO}_2} = 1.45$ and $n_{\text{Si}} = 3.5$ are used. The purpose of inverse design is to separate 1300 nm signal to the upper waveguide and 1500 nm signal to the bottom waveguide.

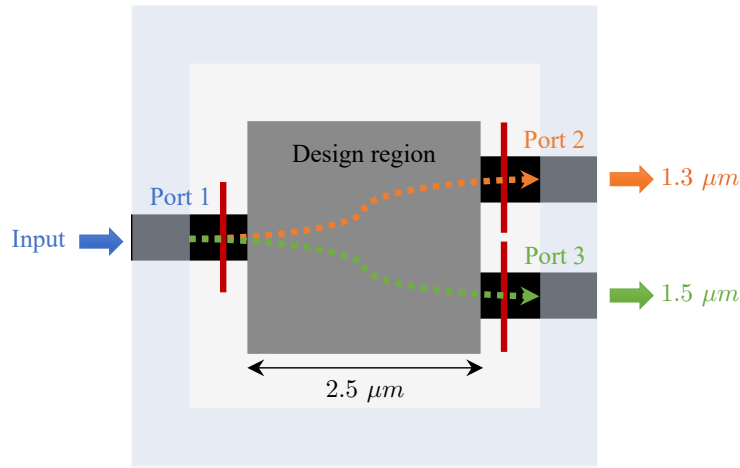


Figure 2: Illustration of wavelength demultiplexer design. The structure consists of one input waveguide (port 1), two output waveguides (port 2 and port 3), and a $2.5 \mu\text{m} \times 2.5 \mu\text{m}$ design region. All three waveguides are the same, with a width of 500 nm. The outer hatched light blue frame represents the simulation domain, specifically, the perfectly matched layer boundaries. The goal of inverse design is route to $1.3 \mu\text{m}$ through the top waveguide and $1.5 \mu\text{m}$ through the bottom waveguide.

In this example, the fundamental first-order mode of the input waveguide is used as the input mode for the inverse design, and the fundamental first-order modes of the two output waveguides are used as the output modes. Initially, the permittivity in design region is homogeneously distributed as shown in Figure 3 (c) and the resulting electric field intensity E_{z_1} at 1500 nm and E_{z_2} at 1300 nm are calculated by FDFD simulations, as shown in Figure 3 (a) and (b) respectively. To conduct the FDFD simulation, the entire structure is discretized by 120×120 pixels and the design region is parametrized by 60×60 pixels, leading to the pixelated design. For ease of inverse design process, we define a relative permittivity ϵ_i with a minimum value $\epsilon_{\text{min}} = 1.0$ (white color in Figure 3 (c)) and maximum value $\epsilon_{\text{max}} = 12.0$ (black color in Figure 3 (c)). The initial permittivity distribution with $\epsilon_{\text{ini}} = 6.5$ are set up for the design region.

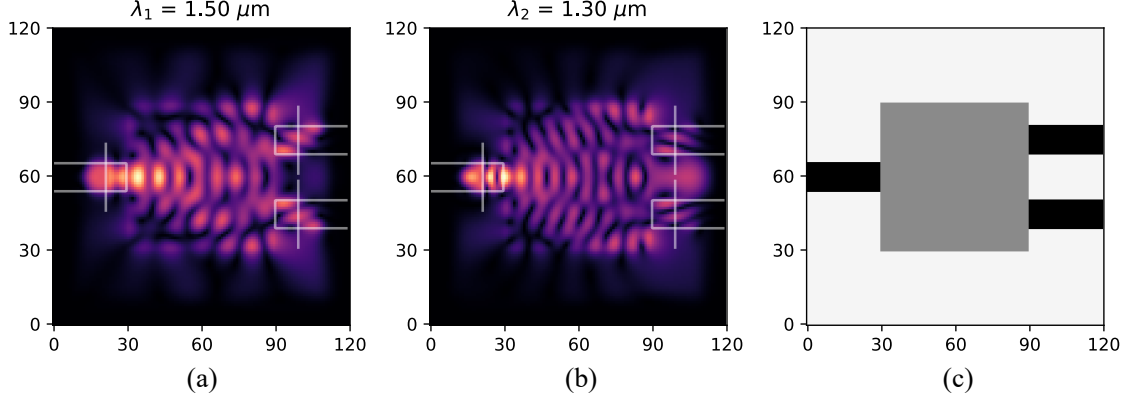


Figure 3: Initialization of inverse design. (a) Electric field intensity at 1500 nm, (b) electric field intensity at 1300 nm, and (c) initial permittivity distribution

4.2. Objective function

We define the output modes of interest as ζ_1 and ζ_2 over output surface S . The device performance is then specified by the overlap integral, which is given by

$$\mathbf{c}^\dagger \mathbf{E}_i(\boldsymbol{\epsilon}(\mathbf{x})) = \iint_S \zeta_i \cdot \mathbf{E}_i(\boldsymbol{\epsilon}(\mathbf{x})) dS \quad (18)$$

where we use it to compute the mode coupling efficiency into each output mode. To achieve the goal of maximum overlap integral, the optimization problem is formulated as follows:

$$\begin{aligned} \min_{\mathbf{x}, \mathbf{E}_1, \mathbf{E}_2} & \quad -\exp [\log(\mathbf{c}^\dagger \mathbf{E}_1) - \log(\mathbf{c}^\dagger \mathbf{E}_{z_1}) + \log(\mathbf{c}^\dagger \mathbf{E}_2) - \log(\mathbf{c}^\dagger \mathbf{E}_{z_2})] \\ \text{subject to} & \quad \nabla \times \frac{1}{\mu} \nabla \times \mathbf{E}_1 - \omega_1^2 \boldsymbol{\epsilon}(\mathbf{x}) \mathbf{E}_1 = -i\omega_1 \mathbf{J}_1 \\ & \quad \nabla \times \frac{1}{\mu} \nabla \times \mathbf{E}_2 - \omega_2^2 \boldsymbol{\epsilon}(\mathbf{x}) \mathbf{E}_2 = -i\omega_2 \mathbf{J}_2 \end{aligned} \quad (19)$$

where ω_1 and ω_2 are the angular frequencies at 1300 and 1500 nm, \mathbf{E}_1 and \mathbf{E}_2 are the electric field, and \mathbf{J}_1 and \mathbf{J}_2 inject input sources into the waveguide for frequency ω_1 and ω_2 . The objective is a sum with four terms using a negative log-sum-exp smooth approximation of the maximum function, and each term corresponds to a sub-objective. As shown in Eq. (19), two terms $\log(\mathbf{c}^\dagger \mathbf{E}_1)$ and $\log(\mathbf{c}^\dagger \mathbf{E}_2)$ correspond to maximizing transmission efficiency through the top waveguide at 1300 nm and bottom waveguide at 1500 nm, given the specific permittivity distribution $\boldsymbol{\epsilon}(\mathbf{x})$, and two terms $\log(\mathbf{c}^\dagger \mathbf{E}_{z_1})$ and $\log(\mathbf{c}^\dagger \mathbf{E}_{z_2})$ correspond to the initial overlap integral given the homogeneous permittivity distribution $\boldsymbol{\epsilon}_{\text{ini}}(\mathbf{x}_{\text{ini}})$, which are mainly used to normalize the objective. One may consider to include other sub-objectives using alternative mathematical formulation for improving the optimization performance. Interested reader

may find more discussion in [11].

4.3. Parameterization scheme

By selecting an appropriate parameterization, the fabrication constraints in optimization can be naturally imposed. The parameterization scheme here consists of two crucial operators: nonlinear projection and convolution filtering. Nonlinear projection aims to binarize the permittivity distribution by

$$\epsilon(\mathbf{x}) = \epsilon_{\min} + (\epsilon_{\max} - \epsilon_{\min})\varphi(\mathbf{x}), \quad \varphi(\mathbf{x}) = \frac{\tanh(\beta \cdot \eta) + \tanh(\beta \cdot (\mathbf{x} - \eta))}{\tanh(\beta \cdot \eta) + \tanh(\beta \cdot (1 - \eta))} \quad (20)$$

where β is the coefficient of projection strength, and η is the center of the projection. Figure 4 (a) shows the nonlinear projected mapping between original input \mathbf{x} and projected $\hat{\mathbf{x}} = \varphi(\mathbf{x})$ given different projection strength and fixed $\eta = 0.5$. As the increasing of projection strength β , the projected $\hat{\mathbf{x}}$ shows a clear trend to binary value 0 or 1.

The convolution operator is used as a blurring filter that results in smooth features of the permittivity distribution and avoids to the tiny features that are less than the minimum feature size of fabrication. Integrating nonlinear projection ($\beta = 50$ and $\eta = 0.5$) and convolution filtering, we visualize the parameterized distribution with varying circle radius based on a specific permittivity distribution, as shown in Figure 4 (b). It is clear to see that the parameterized distribution shows a clear black-white pixel (material layout) without intermediate grey pixels. The feature size can be controlled by determining a specific convolution radius.

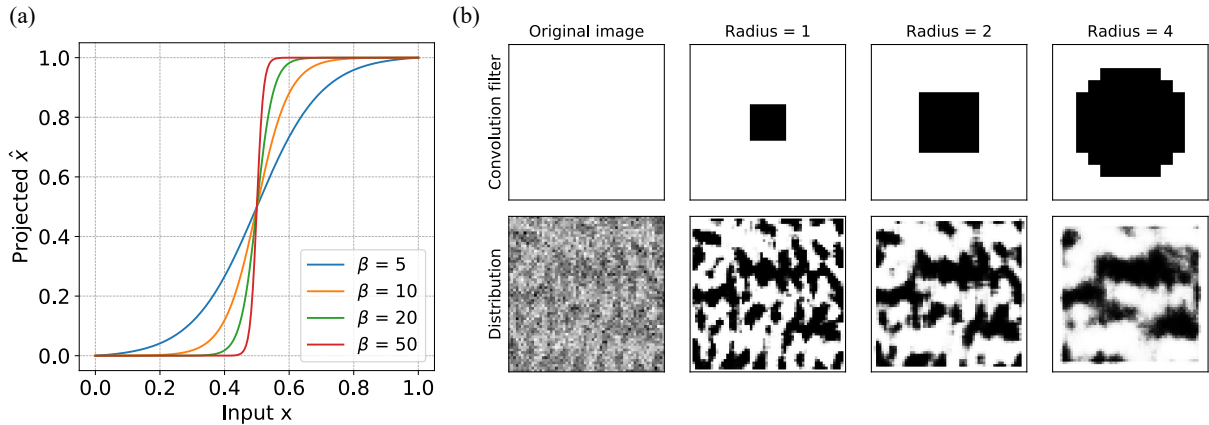


Figure 4: Parameterization scheme for inverse design. (a) Nonlinear projection function for binarizing the input design variables and (b) visualization of convolution filtering with different filter radius given a specific projection strength.

4.4. Methodology workflow

We illustrate a workflow to implement DGS-based nonlocal optimization method for inverse design problem. Figure 5 shows the four core components, that are parameterization, physics simulation, objective formulation and optimization. The detailed procedure is summarized as follows:

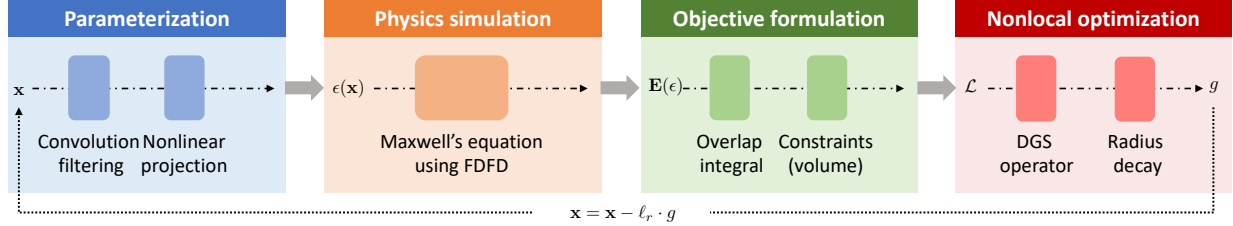


Figure 5: Methodology workflow of inverse design using nonlocal optimization method.

- Step 0: Initialization. An initial design variable \mathbf{x}_0 are set up through a homogeneously distribution or a random distribution with noise.
- Step 1: Parameterization. For design variable \mathbf{x}_k at the k -th iteration, convolution filtering with a specific radius is imposed to eliminate the small features, followed by the nonlinear projection in Eq. (20) that binarizes the design variables. Parameterization builds up a transformation between design variable \mathbf{x}_k and the corresponding permittivity distribution $\epsilon(\mathbf{x}_k)$.
- Step 2: Physics simulation. The permittivity distribution $\epsilon(\mathbf{x}_k)$ are taken as input to physics simulation, for example, electromagnetic simulation. The electric field intensity $\mathbf{E}(\epsilon(\mathbf{x}_k))$ are obtained by solving the Maxwell's equation in Eq. (3) using FDFD method.
- Step 3: Objective formulation. The objective function in Eq. (19) are formulated to conduct the optimization for inverse design. The resulting $\mathbf{E}(\epsilon(\mathbf{x}_k))$ is used to calculate the overlap integral and then yield a scale value \mathcal{L}_k as the loss. The constraints on fabrication and volume fraction are also defined in this step.
- Step 4: Nonlocal optimization. The Step 1-3 can be considered as a forward evaluation where a set of input-output paired samples $\mathbb{S} = \{(\mathbf{x}_k^{(1)}, \mathcal{L}_k^{(1)}), \dots, (\mathbf{x}_k^{(l)}, \mathcal{L}_k^{(l)})\}$ can be drawn for DGS gradient operator. These samples drawn by Gauss-Hermite quadrature rule are used to estimate each directional derivative in Eq. (13) and are then assembled to accurately approximate the full d -dimensional gradient \mathbf{g}_k in Eq. (15). The DGS

gradient is well-suited to update the design variable via gradient descent algorithm:

$$\mathbf{x}_{k+1} = \mathbf{x}_k - \ell_k \cdot \mathbf{g}_k \quad (21)$$

The new design variable \mathbf{x}_{k+1} goes back to Step 1 for iterative updating until the convergence criteria is satisfied.

To improve the optimization performance on accuracy, convergence and robustness, we implement an adaptive decay scheme for updating hyperparameters, including a large DGS radius σ_r in Eq. (13), learning rate ℓ_r in Eq. (21) and projection strength β in Eq. (4). Specifically, the quadratic decay is used

$$z_l = (z^{\text{ini}} - z^{\text{end}}) \times \left(1.0 - \frac{k}{k_{\text{max}}}\right)^\alpha + z^{\text{end}}, \quad (22)$$

where z_l represents the hyperparameters that can be σ_r , ℓ_r or β at the k -th iteration, k_{max} is the maximum of iteration and $\alpha = 2$ is the coefficient of decay rate. z^{ini} and z^{end} are the initial value and end value of hyperparameters respectively. In this study, we use $\sigma_r^{\text{ini}} = 0.25$ and $\sigma_r^{\text{end}} = 0.05$ for DGS radius, $\ell_r^{\text{ini}} = 1.0$ and $\ell_r^{\text{end}} = 0.01$ for learning rate, and $\beta^{\text{ini}} = 0.2$ and $\beta^{\text{end}} = 0.05$ for the reciprocal of projection strength. In addition, the radius $r = 2$ in convolution filtering is used for parameterization. The physics simulation is achieved by *ceviche* (<https://github.com/fancompute/ceviche>) that is an electromagnetic simulation tool for solving Maxwell's equations. In DGS gradient operator, five GH quadrature points are used and the nodes of points in practical computation can be reduced to three due to symmetric property [42]. All numerical experiments (physics simulation and optimization) are implemented in Python 3.6 and conducted on a cluster with 44 Intel Xeon E5-2699 v4 CPUs at 2.20 GHz. Each iteration in optimization takes around 1.2 min using a parallel implementation of DGS gradient operator.

4.5. Result and discussion

The methodology workflow of inverse design is applied here to maximize the performance of nanophotonic devices described in Section 4.1. The final optimized design and the corresponding electric field intensity are diagrammed in Figure 6. Note that the device designed by nonlocal optimization method using DGS gradient, shown in Figure 6 (a), displays a nonintuitive geometry while retaining relatively large features and a clear permittivity distribution with ideal binarization. The light takes a relatively confined path through the structure at both wavelengths. The optimization history, shown in Figure 7, provides iterative changes of the permittivity distribution during the optimization process. Initially,

the permittivity distribution is blurry without a confined path but gradually tends to be clear as the objective value increases. The nonlocal optimization method shows a faster ascending trend initially and converges to a higher objective value using approximate 40 iterations, and finally reach $f_{\text{DGS}}^* = 13.58$, that performs $\sim 10\%$ improvement compared with the local gradient method that is $f_{\text{local}}^* = 12.38$ using 100 iterations. It can be seen that the local gradient method shows significant oscillations at 50 and 75 iterations, shown in Figure 7. This is mainly due to the fact that the projection strength is increased by a discrete step function in the classical local gradient method. The nonlocal optimization method using DGS gradient shows a relatively smoothing iteration curve since a dynamic decay mechanism is implemented to adaptively update the projection strength. The gap at the final objective values between the nonlocal optimization method and the local gradient method is also demonstrated by the optimized design and the resulting electric field intensity in Figure 6. It is easy to observe that the light path in local gradient design, specifically at 1500 nm wavelength (left in Figure 6(b)) is relatively diffused. Note that, the performance of the local gradient method might be improved through a long run but in order to fairly compare, we terminate the optimization by 100 iterations for both methods.

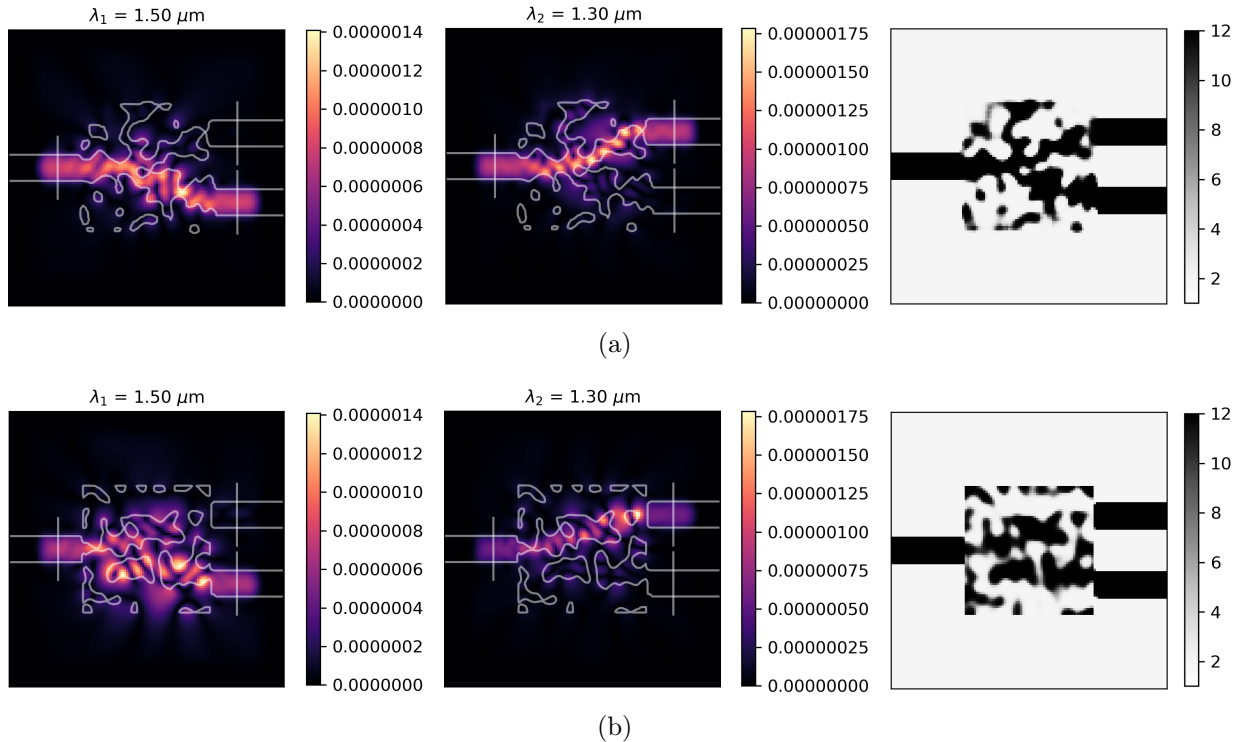


Figure 6: Electric field intensity of the optimized device at 1500 nm (left column) and 1300 nm (middle column), as well as the optimized permittivity distribution (right column) using (a) nonlocal optimization method with DGS gradient and (b) local gradient based optimization

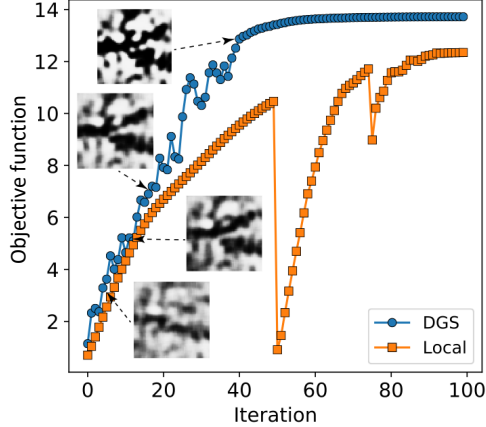


Figure 7: The optimization iteration history. The blue circles represent the optimization using DGS gradient operator and the orange squares represent the optimization using local gradient algorithm.

4.5.1. Effect of random initialization with Gaussian noise

Here we investigate the effect of random initialization on the optimized permittivity distribution and device performance. In this case, we repeatably run 100 times optimization with three different levels of randomness described by Gaussian noise: $N(0, 0.1)$, $N(0, 0.05)$ and $N(0, 0.01)$. The iteration history and histogram of final objective values are shown in Figure 8 and Figure 9. The solid curves in Figure 8 represent the mean value of 100 trials and the dash area represents the confidence intervals with $[-\sigma, +\sigma]$, where σ is the standard deviation of the objective values at a specific iteration. It can be seen that the variation of objective value is relatively large but it is quickly narrowed and converged to the final value, which is pretty close in all three levels of randomness. The histogram in Figure 9 shows the distribution of the final objective values using the nonlocal optimization method with DGS gradient (dark color) and local gradient (light color). The nonlocal method outperforms the local gradient in terms of the objective values and shows a smaller variation in all three levels of randomness. Table 1 provides a statistical comparison of objective values between nonlocal method using DGS gradient and local gradient methods. Compared with the local gradient method, the nonlocal optimization method shows superior performance with an improvement of 9.37%, 9.42%, and 9.22% in the mean value respectively. For the standard deviation, two methods show almost the same variation level if the noise is tiny, specifically at $\sigma_N = 0.01$ but the nonlocal optimization method using DGS gradient achieves a significant reduction of 21.1% and 30.6% when the noise level is relatively large, typically at $\sigma_N = 0.1$ and $\sigma_N = 0.05$. Through a statistical analysis of the objective values, the nonlocal optimization method shows a higher objective value and much smaller uncertainty on the final performance, particularly given relatively large randomness associated with the initial conditions. In other words, the

nonlocal optimization method demonstrates stronger robustness and reliability to resist the local minima caused by random initialization.

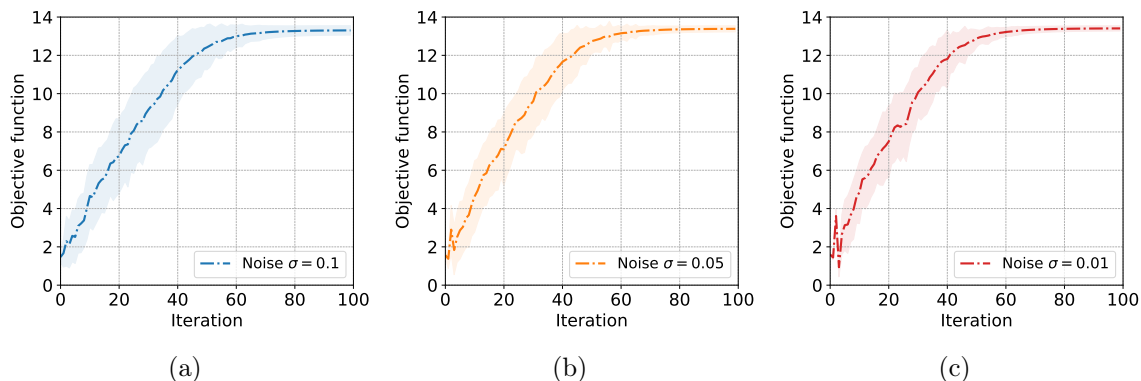


Figure 8: Study of the local minima with three initialization with random Gaussian noise for the inverse design performance. The optimization is run 100 times with random initial conditions (different random seeds). (a) Gaussian noise $N(0, 0.1)$, (b) Gaussian noise $N(0, 0.05)$ and (c) Gaussian noise $N(0, 0.01)$.

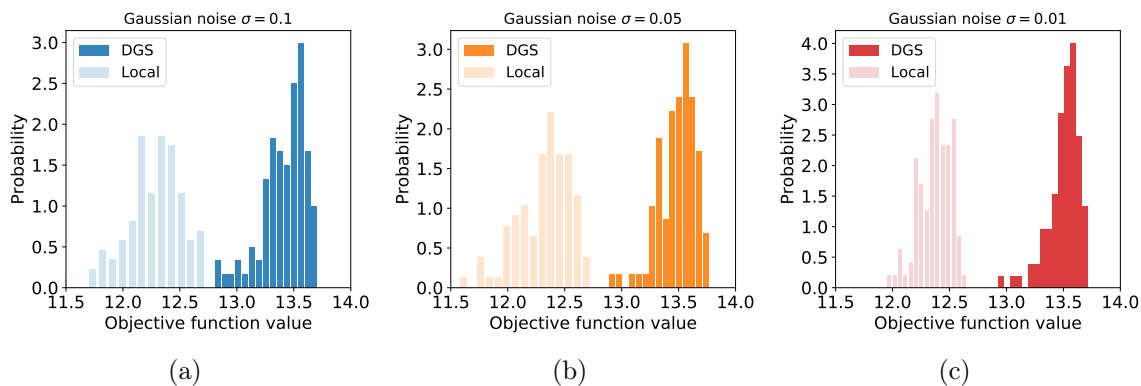


Figure 9: Histogram of the objective function values of 100 local minima given different noise levels. Dark color represents the distribution using the nonlocal optimization method with DGS gradient and light color represents the distribution using local gradient algorithm. (a) Gaussian noise $N(0, 0.1)$, (b) Gaussian noise $N(0, 0.05)$ and (c) Gaussian noise $N(0, 0.01)$.

Table 1: Statistical comparison of optimized performance between the nonlocal optimization method with DGS gradient and local gradient method

	Nonlocal optimization		Local gradient	
Gaussian noise	Mean	Standard deviation	Mean	Standard deviation
$\sigma_N = 0.1$	13.42	0.191	12.27	0.242
$\sigma_N = 0.05$	13.48	0.159	12.32	0.229
$\sigma_N = 0.01$	13.51	0.136	12.37	0.141

Figure 10 - Figure 12 show a sample collection of optimized design with the electric field intensity given Gaussian noise $N(0, 0.1)$, $N(0, 0.05)$ and $N(0, 0.01)$ respectively. For a specific

noise level, three selected samples are provided, and each of samples corresponds to a random initial condition (first column), DGS-based nonlocal optimized design (column 2) with the electric field intensity at 1500 nm wavelength (column 3) and 1300 nm wavelength (column 4), as well as the local gradient-based design (column 6) with the electric field intensity at 1500 nm wavelength (column 7) and 1300 nm wavelength (column 8). In particular, when the noise level is relatively high, as shown in Figure 10, the optimized structure using DGS gradient shows a clear binary distribution with an overall consistent pattern, while some small features and differences exist. The corresponding electric field shows a similar confined and clear transmission path. However, the optimized design using the local gradient method greatly varies with the random initialization. It is difficult to see a clear path as several noise features are embedded into the structure. This results in the fact that the electric field spreads across the entire device, suggesting that multi-path interference contributes to the device performance that is unexpected. This is because the local gradient method is limited to escape the local minima that strongly depend on the initial conditions. Although noise level is decreased from $N(0, 0.1)$ to $N(0, 0.05)$, as shown in Figure 11, the local gradient method is still affected by the initial random noise. As a result, the optimized structure includes a few small features with noise and the overall structure is unstable and unclear. On the contrary, the nonlocal optimization method is well-suited to handle the noise using a Gaussian smoothing operator with a large radius and thus achieves a robust and binarized design. When a small noise is imposed into the initialization, three samples from the nonlocal optimization method with DGS gradient in Figure 12 are almost identical and converged to the optimized design as similar as the result using homogeneous initialization without any randomness. For the local gradient method, the noised feature is mitigated from the optimized structure but the resulting electric field intensity still underperforms the nonlocal method, specifically at the 1500 nm.

4.5.2. Inverse design optimization with volume constraint

The optimized design discussed above is achieved by optimization without any constraint of materials usage. To investigate the effect of material usage on device performance, we conduct a study to investigate the relationship between volume fraction of material usage and objective function values, as shown in Figure 13. A total of 300 samples of three levels of Gaussian noise are used in this case but unfortunately, we didn't observe a strong correlation between the volume fraction and final objective values. Most cases of volume fraction in Figure 13 concentrates in 0.45–0.65 and no cases are lower than 0.35. It naturally gives rise to an interesting question: is that possible to use fewer materials but achieve equivalently good performance?

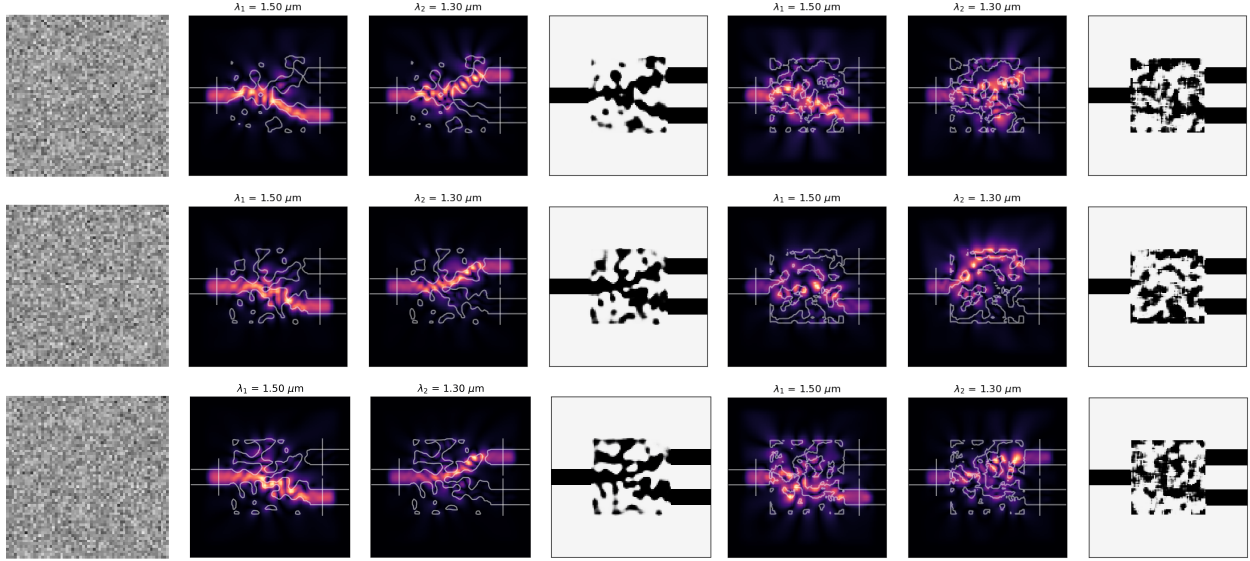


Figure 10: A sample collection of optimized permittivity distribution and the corresponding electric field intensity given initial Gaussian noise $N(0, 0.1)$.

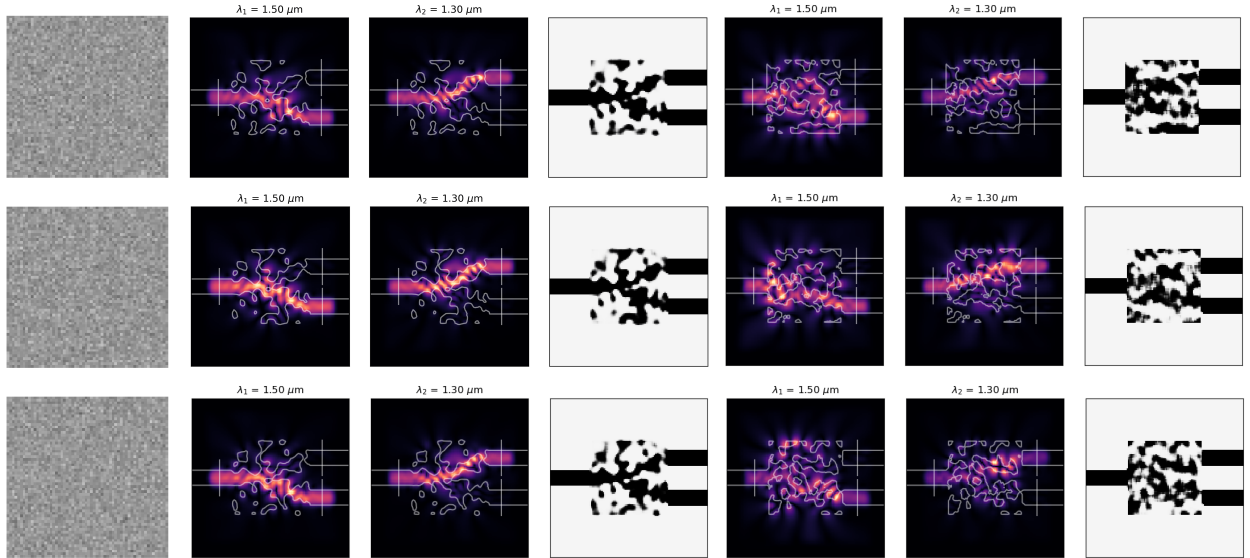


Figure 11: A sample collection of optimized permittivity distribution and the corresponding electric field intensity given initial Gaussian noise $N(0, 0.05)$.

To answer this question, we reformulate the optimization by adding a volume constraint and solve this constrained optimization problem using the Method of Moving Asymptotes (MMA) [46]. However, MMA is limited to seek optima using local gradients, either via adjoint method or finite difference. We address this challenge by inserting the DGS gradient into the MMA optimizer so that we can exploit the nonlocal exploration of the DGS operator to search for a better design. Figure 14 shows the optimized design with volume constraint

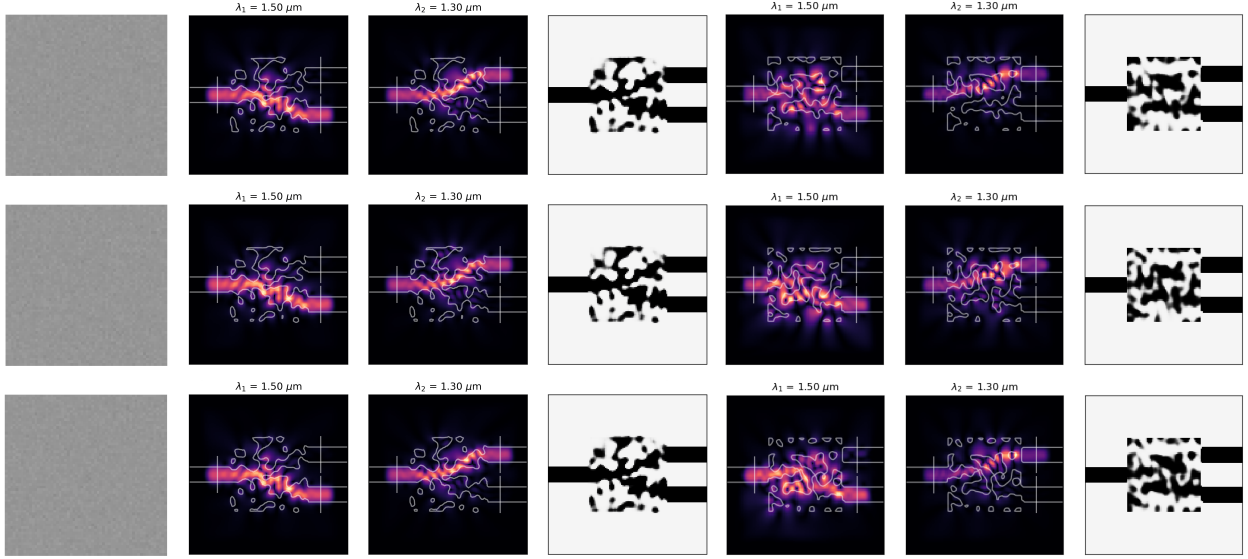


Figure 12: A sample collection of optimized permittivity distribution and the corresponding electric field intensity given initial Gaussian noise $N(0, 0.01)$.

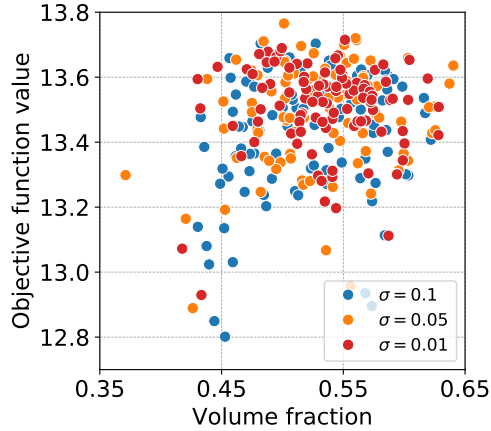


Figure 13: Relationship between volume fraction and optimized objective value under random initialization. There is no clear correlation between the used amount of materials and the optimized performance.

$\gamma = 0.3$ that means only 30% of materials in the design domain are used. We easily observe a clear and confined light transmission path at both 1500 nm and 1300 nm. The optimized permittivity distribution shows the fundamental splitter-like feature and eliminates a lot of unnecessary material in the device compared with the design without volume constraint.

Figure 15 shows the iteration history of constrained optimization with $\gamma = 0.3$. To illustrate the optimized process in detail, Figure 15 (a) shows the iterative change of electric field intensity at 1500 nm and the objective value that corresponds the term $\exp [\log(\mathbf{c}^\dagger \mathbf{E}_1) - \log(\mathbf{c}^\dagger \mathbf{E}_{z_1})]$ in objective function (see Eq. (19)) . Similarly, the iteration history of objective term $\exp [\log(\mathbf{c}^\dagger \mathbf{E}_2) - \log(\mathbf{c}^\dagger \mathbf{E}_{z_2})]$ at 1300 nm is shown in Figure 15 (b). Note that, under the

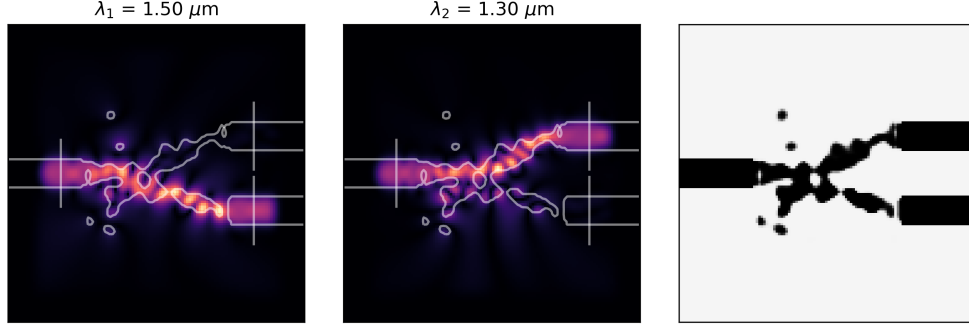


Figure 14: Optimized device with volume constraint $\gamma = 0.3$. The electric field intensity of the optimized device at 1500 nm (left) and at 1300 nm (middle), as well as the optimized permittivity distribution (right) using DGS gradient with MMA optimizer

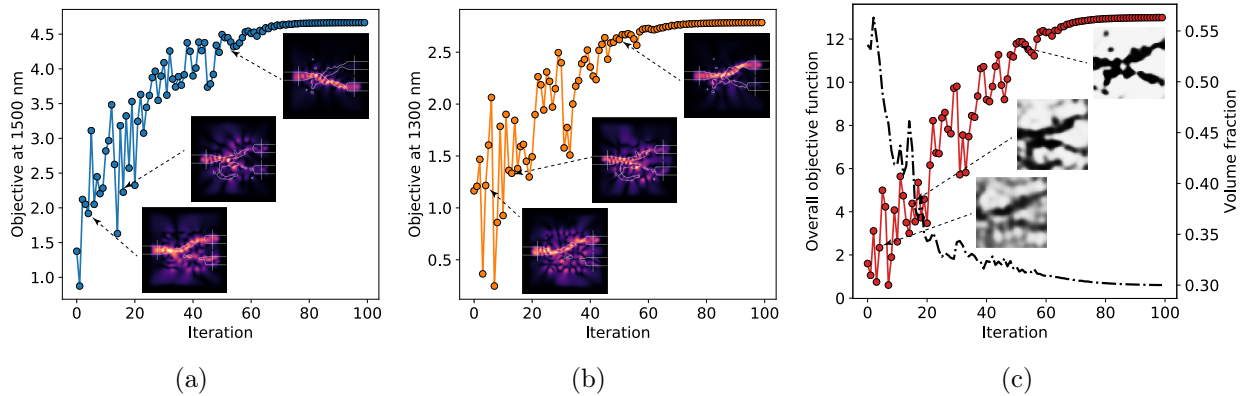


Figure 15: Iteration history of constrained optimization with $\gamma = 0.3$ and the corresponding electrical field intensity and permittivity distribution. (a) Objective at 1500 nm, (b) objective at 1300 nm and (c) overall objective and volume fraction iteration.

volume fraction constraint, the iteration curves show some oscillations initially but quickly converge at the 60th iteration. The designed device successfully separates both signals at the assigned port. Figure 15 (c) shows the iteration history of overall objective (red color), the decay of volume fraction (black color) and the changes of permittivity distribution. The constrained optimization using DGS gradient integrating with MMA optimizer achieves a nearly same high performance, $f_{\text{DGS}}^{0.3} = 13.09$ as the optimization without volume constraint. But the amount of material usage is significantly reduced from 0.474 (the case in Figure 6(a)) to 0.3 and we therefore save 36.7% material usage.

We further reduce the volume fraction from 0.3 to 0.2 to exploit the maximizing capability of the nonlocal method using DGS gradient integrating with the MMA optimizer. Figure 16 shows the electric field intensity based on the optimized permittivity distribution given $\gamma = 0.2$. The optimized design still retains the principle splitter-like features that connect the input port and two output ports, even though a very limited amount of material is used. As

similar to the optimized design with $\gamma = 0.3$, few small spots are disconnected from the main structure and probably play a limited role in the effective transmission of the input source. This special feature, observed by several previous studies [10, 37, 20, 11] is probably due to the issue of local minima. Although DGS operator enables nonlocal exploration to facilitate the global search, the optimized devices may be trapped into one of the local minima.

Figure 15 shows the iterative process of constrained optimization. It is noted that the iteration history at 1500 nm (Figure 15 (a)) and 1300 nm (Figure 15 (b)) shows a relatively large oscillation, specifically in the initial stage. This probably results from the fast decay of volume fraction in the initial period, as shown in Figure 15 (c). After 60 iterations, the objective values tend to converge and the volume fraction also approaches to the constrained value, $\gamma = 0.2$. This case with a smaller volume fraction achieves a final objective value $f_{\text{DGS}}^{0.2} = 12.70$ that is slightly lower ($\sim 3.71\%$) than the case of $\gamma = 0.3\%$ but saves 33.3% material usage.

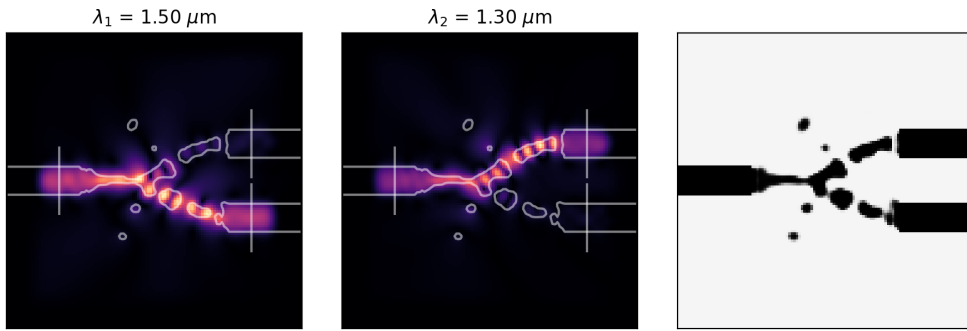


Figure 16: Optimized device with volume constraint $\gamma = 0.2$. The electric field intensity of the optimized device at 1500 nm (left) and at 1300 nm (middle), as well as the optimized permittivity distribution (right) using DGS gradient with MMA optimizer

The final designed devices with three different amounts of material usage are shown in Figure 18. From the angled view, the vertical sidewalls are clearly visible and the permittivity distribution along the vertical direction are all same. This is easy for fabricating using electron-beam (top-down) lithography followed by etching the 220-nm-thick layer of an SOI substrate, leaving the structure with an air cladding. Compared with the classical design approaches, the proposed inverse design framework integrating the DGS gradient with MMA optimizer provides higher final performance with less material usage for real fabrication in practice.

5. Conclusion

This work focuses on the development of a nonlocal optimization method for computational inverse design in nanophotonics. A novel DGS gradient operator is introduced to improve

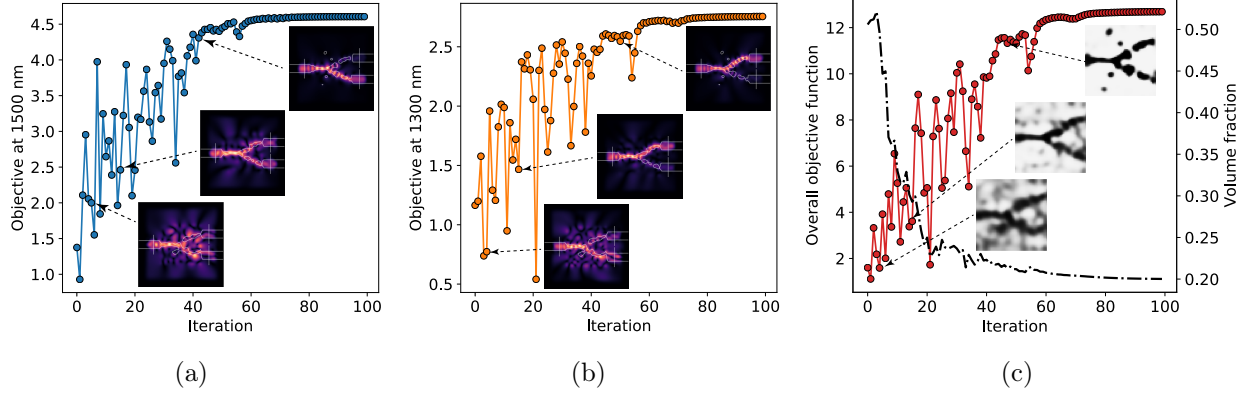


Figure 17: Iteration history of constrained optimization with $\gamma = 0.2$ and the corresponding electrical field intensity and permittivity distribution. (a) Objective at 1500 nm, (b) objective at 1300 nm and (c) overall objective and volume fraction iteration.

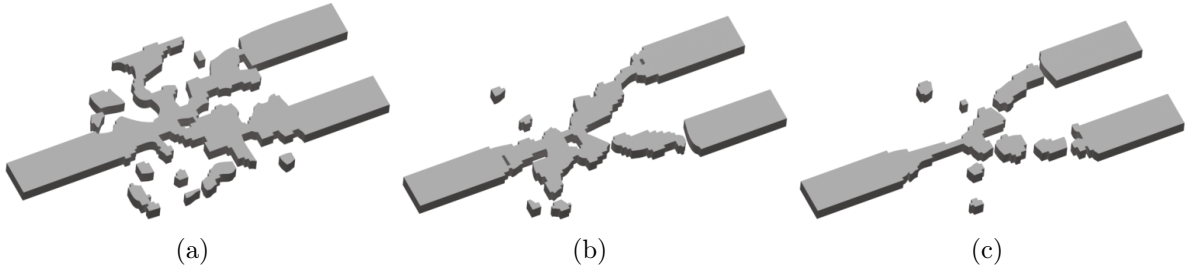


Figure 18: A three-dimensional rendering of the optimized design. Silicon is shown in grey and light enters the optimized device from the input waveguide on the left-hand side (port 1) and exits via one of the two output waveguides (port 2 and port 3) on the right side. There are three optimized devices with different volume fraction (a) $\gamma = 0.474$, (b) $\gamma = 0.3$ and (c) $\gamma = 0.2$.

the nonlocal exploration capability required for escaping from local minima in the high-dimensional non-convex landscapes. The DGS gradient operator is achieved by conducting 1D nonlocal explorations along with d orthogonal directions in \mathbb{R}^d , each of which defines a nonlocal directional derivative as a 1D integral. Instead of Monte Carlo (MC) sampling, a deterministic Gauss-Hermite (GH) quadrature is used to estimate each of 1D integrals in d -dimension to achieve high accuracy. Compared with the local gradient method, the directional smoothing allows for a large smoothing radius to capture the global structure of loss landscapes. GH quadrature with error bound provides guarantees higher accuracy than random sampling, even though a large smoothing radius is used.

The nonlocal optimization method using DGS gradient has advantages in portability and flexibility so that it is naturally incorporated with parameterization, physics simulation, and objective formulation to build up an effective optimization workflow for inverse design. Within the nonlocal optimization scheme, an adaptive smoothing radius and learning rate with quadratic decay is proposed to accelerate the convergence and improve the robustness by

reducing the dependence of optimized design on random initialization. To make the optimized design easy to fabrication, a dynamic growth mechanism is imposed on the projection strength in parameterization to achieve a clear material layout. Moreover, we investigate the effect of material usage on optimized performance by integrating the DGS gradient with MMA optimizer to conduct a nonlocal constrained optimization with adding volume constraint into optimization formulation.

The proposed method is demonstrated on a wavelength demultiplexer design problem that aims to split 1500 nm and 1300 nm signals from an input waveguide into two output waveguides. The results show that the proposed inverse design framework using nonlocal optimization method achieves an improvement of approximate 10% performance with faster convergence compared with the classical local gradient-based approaches. Given different levels of the random initial condition, the DGS-based nonlocal method presents a smaller variation and higher robustness on the final optimized design. Optimization with volume constraint demonstrates the final optimized device can maintain the high performance as similar to the optimized design without volume concern but achieves a significant reduction (36.7% for $\gamma = 0.3$ and 57.8% for $\gamma = 0.2$) of material usage.

Future work may potentially explore the effect of different types of random initial conditions on the local minima. The current study only addresses the Gaussian noise with different standard deviation to the initial condition. It would be interesting to study the other types of random noise, for example, Perlin noise and Gabor noise as suggested in [11]. Besides, the optimized devices are composed of a small number of distinct spot materials, which may play an uncertain role in light transmission and separation. We plan to make a further investigation on the reason for these small features and explore their effect on the performance of electric field intensity, specifically when volume fraction is relatively low.

6. Acknowledgements

This work was supported by the U.S. Department of Energy, Office of Science, Office of Advanced Scientific Computing Research, Applied Mathematics program under contract ERKJ352; and by the Artificial Intelligence Initiative at the Oak Ridge National Laboratory (ORNL). ORNL is operated by UT-Battelle, LLC., for the U.S. Department of Energy under Contract DEAC05-00OR22725.

References

- [1] L. A. Coldren, S. W. Corzine, M. L. Mashanovitch, Diode lasers and photonic integrated circuits, volume 218, John Wiley & Sons, 2012.

- [2] D. A. Miller, Optical interconnects to electronic chips, *Applied optics* 49 (2010) F59–F70.
- [3] V. S.-Y. Lin, K. Motesharei, K.-P. S. Dancil, M. J. Sailor, M. R. Ghadiri, A porous silicon-based optical interferometric biosensor, *Science* 278 (1997) 840–843.
- [4] B. Kress, T. Starner, A review of head-mounted displays (hmd) technologies and applications for consumer electronics, in: *Photonic Applications for Aerospace, Commercial, and Harsh Environments IV*, volume 8720, International Society for Optics and Photonics, p. 87200A.
- [5] P. Kok, W. J. Munro, K. Nemoto, T. C. Ralph, J. P. Dowling, G. J. Milburn, Linear optical quantum computing with photonic qubits, *Reviews of Modern Physics* 79 (2007) 135.
- [6] A. Polman, H. A. Atwater, Photonic design principles for ultrahigh-efficiency photovoltaics, *Nature materials* 11 (2012) 174–177.
- [7] S. Molesky, Z. Lin, A. Y. Piggott, W. Jin, J. Vucković, A. W. Rodriguez, Inverse design in nanophotonics, *Nature Photonics* 12 (2018) 659–670.
- [8] D. Wu, C. Liu, Z. Xu, Y. Liu, Z. Yu, L. Yu, L. Chen, R. Li, R. Ma, H. Ye, The design of ultra-broadband selective near-perfect absorber based on photonic structures to achieve near-ideal daytime radiative cooling, *Materials & Design* 139 (2018) 104–111.
- [9] K. Y. Yang, J. Skarda, M. Cotrufo, A. Dutt, G. H. Ahn, M. Sawaby, D. Verdecruyse, A. Arbabian, S. Fan, A. Alù, et al., Inverse-designed non-reciprocal pulse router for chip-based lidar, *Nature Photonics* 14 (2020) 369–374.
- [10] A. Y. Piggott, J. Lu, K. G. Lagoudakis, J. Petykiewicz, T. M. Babinec, J. Vucković, Inverse design and demonstration of a compact and broadband on-chip wavelength demultiplexer, *Nature Photonics* 9 (2015) 374–377.
- [11] L. Su, D. Verdecruyse, J. Skarda, N. V. Sapra, J. A. Petykiewicz, J. Vucković, Nanophotonic inverse design with SPINS: Software architecture and practical considerations, *Applied Physics Reviews* 7 (2020).
- [12] J. Peurifoy, Y. Shen, L. Jing, Y. Yang, F. Cano-Renteria, B. G. DeLacy, J. D. Joannopoulos, M. Tegmark, M. Soljačić, Nanophotonic particle simulation and inverse design using artificial neural networks, *Science Advances* 4 (2018) 1–8.

- [13] J. S. Jensen, O. Sigmund, Topology optimization for nano-photonics, *Laser & Photonics Reviews* 5 (2011) 308–321.
- [14] G. Angeris, J. Vučković, S. P. Boyd, Computational Bounds for Photonic Design, *ACS Photonics* 6 (2019) 1232–1239.
- [15] T. Phan, D. Sell, E. W. Wang, S. Doshay, K. Edee, J. Yang, J. A. Fan, High-efficiency, large-area, topology-optimized metasurfaces, *Light: Science & Applications* 8 (2019) 1–9.
- [16] L. H. Frandsen, Y. Elesin, L. F. Frellsen, M. Mitrovic, Y. Ding, O. Sigmund, K. Yvind, Topology optimized mode conversion in a photonic crystal waveguide fabricated in silicon-on-insulator material, *Optics express* 22 (2014) 8525–8532.
- [17] T. W. Hughes, M. Minkov, I. A. Williamson, S. Fan, Adjoint Method and Inverse Design for Nonlinear Nanophotonic Devices, *ACS Photonics* 5 (2018) 4781–4787.
- [18] D. Yan, L. Qiu, M. Xue, Z. Meng, Y. Wang, A flexible surface-enhanced raman substrates based on cellulose photonic crystal/ag-nanoparticles composite, *Materials & Design* 165 (2019) 107601.
- [19] L. F. Frellsen, Y. Ding, O. Sigmund, L. H. Frandsen, Topology optimized mode multiplexing in silicon-on-insulator photonic wire waveguides, *Optics express* 24 (2016) 16866–16873.
- [20] L. Su, A. Y. Piggott, N. V. Sapra, J. Petykiewicz, J. Vučković, Inverse Design and Demonstration of a Compact on-Chip Narrowband Three-Channel Wavelength Demultiplexer, *ACS Photonics* 5 (2018) 301–305.
- [21] J. Jiang, J. A. Fan, Simulator-based training of generative neural networks for the inverse design of metasurfaces, *Nanophotonics* 1 (2019).
- [22] J. S. Jensen, O. Sigmund, Systematic design of photonic crystal structures using topology optimization: Low-loss waveguide bends, *Applied physics letters* 84 (2004) 2022–2024.
- [23] P. I. Borel, A. Harpøth, L. H. Frandsen, M. Kristensen, P. Shi, J. S. Jensen, O. Sigmund, Topology optimization and fabrication of photonic crystal structures, *Optics express* 12 (2004) 1996–2001.
- [24] T. W. Hughes, I. A. Williamson, M. Minkov, S. Fan, Forward-mode differentiation of maxwell’s equations, *ACS Photonics* 6 (2019) 3010–3016.

- [25] M. Minkov, I. A. Williamson, L. C. Andreani, D. Gerace, B. Lou, A. Y. Song, T. W. Hughes, S. Fan, Inverse design of photonic crystals through automatic differentiation, *ACS Photonics* (2020).
- [26] Y. Jiao, S. Fan, D. A. Miller, Systematic photonic crystal device design: global and local optimization and sensitivity analysis, *IEEE journal of quantum electronics* 42 (2006) 266–279.
- [27] Y. Elesin, B. S. Lazarov, J. S. Jensen, O. Sigmund, Design of robust and efficient photonic switches using topology optimization, *Photonics and nanostructures-Fundamentals and Applications* 10 (2012) 153–165.
- [28] S. D. Campbell, D. Sell, R. P. Jenkins, E. B. Whiting, J. A. Fan, D. H. Werner, Review of numerical optimization techniques for meta-device design, *Optical Materials Express* 9 (2019) 1842–1863.
- [29] D. Vercruyssen, N. V. Sapra, L. Su, R. Trivedi, J. Vučković, Analytical level set fabrication constraints for inverse design, *Scientific reports* 9 (2019) 1–7.
- [30] A. Y. Piggott, J. Petykiewicz, L. Su, J. Vučković, Fabrication-constrained nanophotonic inverse design, *Scientific reports* 7 (2017) 1–7.
- [31] A. Christ, H. L. Hartnagel, Three-dimensional finite-difference method for the analysis of microwave-device embedding, *IEEE Transactions on Microwave Theory and Techniques* 35 (1987) 688–696.
- [32] D. M. Sullivan, *Electromagnetic simulation using the FDTD method*, John Wiley & Sons, 2013.
- [33] O. Sigmund, J. Petersson, Numerical instabilities in topology optimization: a survey on procedures dealing with checkerboards, mesh-dependencies and local minima, *Structural optimization* 16 (1998) 68–75.
- [34] A. Y. Piggott, J. Petykiewicz, L. Su, J. Vučković, Fabrication-constrained nanophotonic inverse design, *Scientific Reports* 7 (2017) 1–7.
- [35] D. Vercruyssen, N. V. Sapra, L. Su, R. Trivedi, J. Vučković, Analytical level set fabrication constraints for inverse design, *Scientific Reports* 9 (2019) 1–7.
- [36] G. Zhang, J. Zhang, J. Hinkle, Learning nonlinear level sets for dimensionality reduction in function approximation, in: *Advances in Neural Information Processing Systems*, pp. 13220–13229.

- [37] T. W. Hughes, M. Minkov, I. A. Williamson, S. Fan, Adjoint method and inverse design for nonlinear nanophotonic devices, *ACS Photonics* 5 (2018) 4781–4787.
- [38] A. G. Baydin, B. A. Pearlmutter, A. A. Radul, J. M. Siskind, Automatic differentiation in machine learning: a survey, *The Journal of Machine Learning Research* 18 (2017) 5595–5637.
- [39] A. Paszke, S. Gross, S. Chintala, G. Chanan, E. Yang, Z. DeVito, Z. Lin, A. Desmaison, L. Antiga, A. Lerer, Automatic differentiation in pytorch (2017).
- [40] J. Zhang, H. Tran, D. Lu, G. Zhang, A Novel Evolution Strategy with Directional Gaussian Smoothing for Blackbox Optimization, *arXiv e-prints* (2020) arXiv:2002.03001.
- [41] Y. Nesterov, V. Spokoiny, Random gradient-free minimization of convex functions, *Foundations of Computational Mathematics* 17 (2017) 527–566.
- [42] A. Quarteroni, R. Sacco, F. Saleri, *Numerical Mathematics*, volume 332, Springer Science Business Media &, 2007.
- [43] M. Abramowitz, I. Stegun (Eds.), *Handbook of Mathematical Functions*, Dover, New York, 1972.
- [44] M. El-Abd, Black-box optimization benchmarking for noiseless function testbed using artificial bee colony algorithm, in: *Proceedings of the 12th Annual Conference Companion on Genetic and Evolutionary Computation, GECCO '10*, Association for Computing Machinery, New York, NY, USA, 2010, p. 1719–1724.
- [45] M. Jamil, X.-S. Yang, A literature survey of benchmark functions for global optimisation problems, *IJMNO* 4 (2013) 150–194.
- [46] K. Svanberg, The method of moving asymptotes—a new method for structural optimization, *International journal for numerical methods in engineering* 24 (1987) 359–373.